

Demonstration of a Logical Architecture Uniting Motion and In-Place Entanglement: Shor's Algorithm, Constant-Depth CNOT Ladder, and Many-Hypercube Code

Infleqtion and Collaborators
(Dated: September 17, 2025)

Logical qubits are considered an essential component for achieving utility-scale quantum computation. Multiple recent demonstrations of logical qubits on neutral atoms have relied on coherent qubit motion into entangling zones. However, this architecture requires motion prior to every entangling gate, incurring significant cost in wall clock runtime and motion-related error accumulation. We propose and experimentally realize an alternative architecture which unites qubit motion and in-place entanglement via nearest-neighbor gates. Our approach maintains all-to-all connectivity, while minimizing qubit motion overheads. We demonstrate three key results on Infleqtion's Sqale QPU, which hosts an array of 114 neutral atom qubits. First, we perform a logical qubit realization of a pre-compiled variant of Shor's Algorithm. We find better logical-than-physical performance over a range of settings including with loss correction and leakage detection. Second, we introduce a technique for performing CNOT ladders with depth independent of both the number of logical qubits N and the code distance d . In proof-of-principle experiments with 8 and 12 logical qubits, we find $\sim 4x$ reduction in error via the logical encodings. Third, we experimentally realize initialization of the $[[16, 4, 4]]$ many-hypercube QEC code. All three results benefit from optimized compilation via Superstaq, as well as our underlying architecture uniting motion and in-place entanglement. This architecture offers a path to reducing the overhead of utility-scale quantum applications relative to architectures based on entangling zones.

I. INTRODUCTION

In the past few years, multiple experiments have achieved control of logical qubits [1–7]. Most of the experiments leverage non-local qubit connectivity to achieve significant milestones such as high-rate quantum error correction codes, efficient magic state preparation, universal gatesets, and code switching. The demonstrations that leverage non-local connectivity typically perform two-qubit physical operations with an architecture that moves qubits into an entanglement zone. Although the zone-based architecture lowers the requirements for efficient classical control and gate calibration [8], it is not yet clear if it will satisfy the threshold theorem for large-scale fault-tolerant quantum computation [9]. In this paper, we realize an alternative neutral atom architecture that unites qubit motion with individual optical addressing for in-place entangling operations. This approach was demonstrated recently on a small scale with physical qubits [10] and is here extended to logical qubit (LQ) encodings. The architecture maintains all-to-all connectivity, while minimizing the pitfalls associated with atom motion like runtime cost and error accumulation.

We demonstrate the benefits of this architecture by experimentally executing multiple circuits on Infleqtion's Sqale QPU that show primitives on the path to utility-scale quantum computing. The remainder of this paper is structured as follows:

- Section II describes the methods underpinning the Sqale architecture from a software & hardware perspective.
- Section III describes the pre-compiled Shor's Algorithm circuits [11] executed with logical qubits on hardware, including with loss correction and with

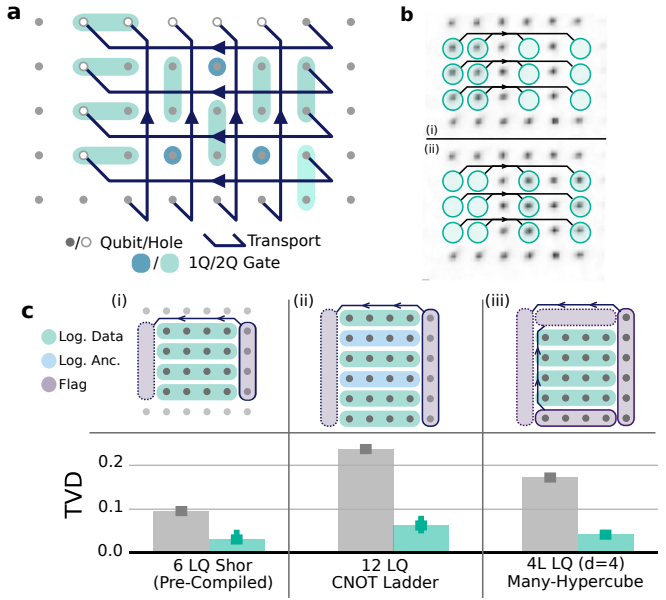


FIG. 1. (a) Sqale's architecture, combining locally-addressed gates and mid-circuit rearrangement. (b) Fluorescence images before (top) and after (bottom) translating and stretching a 6-qubit block through interstitial lanes. (c) Summary of demonstrations in this work. Upper panel: logical qubit layout and mid-circuit reconfigurations for (i, ii) $[[4,2,2]]$ -encoded demonstration of Shor's algorithm and a constant-depth CNOT ladder, and (iii) state-preparation in the $[[16,4,4]]$ many-hypercube code. Lower panel: Encoded/unencoded performance in terms of Total Variation Distance (TVD).

leakage detection. This constitutes the first demonstration of Shor's Algorithm on logical qubits, although we emphasize that the pre-compiled circuits are unscalable.

- Section IV describes a novel technique for implementing logical constant-depth CNOT ladders, with no depth dependence on either the number of logical qubits N or the code distance d of the system. The CNOT ladder circuits leverage ancilla logical qubits and transversal gates. We show proof-of-principle experiments with up to 12 logical qubits.
- Section V describes the execution of state preparation under the level-2 $[[4^L, 2^L, 2^L]]$ many-hypercube code [12], which forms a $[[16, 4, 4]]$ code.
- Section VI presents a broad reflection on how the experiments that were performed herein contribute to the architectural principles for neutral atom quantum computing. Section VII concludes.

These experiments serve as stepping stones towards running utility-scale applications on quantum computers, such as elucidating the properties of optoelectronic materials [13]. For instance, the pre-compiled Shor’s Algorithm circuit is a Hadamard test, which is a crucial primitive for some strongly correlated electron models (such as the Anderson impurity model) [13]. In turn, the Trotterized implementation of the Anderson impurity Hamiltonian will benefit from the constant depth CNOT ladders [14], and the many-hypercube code is a contender for low-overhead utility-scale quantum computation [15].

II. METHODS

A. Movement

In this work, we demonstrate the added capability of mid-circuit atom-rearrangement on top of a neutral platform with individual optical addressability and non-destructive qubit readout [16]. Mid-circuit atom rearrangement enables all-to-all connectivity [8]. In the context of our demonstrations, this capability enables fault-tolerant initialization with flag qubits, transversal entangling logic, and circuit-based leakage detection that would otherwise be challenging with typical planar connectivity. Specifically, our experiments leverage block (parallel) atom motion to achieve the necessary connectivities—typically ring or torus. Once atom motion is performed, several CZ gates are subsequently performed in-place, without necessitating motion to an entangling zone. As such, our experiments exemplify the potential of our underlying architecture, which uses motion sparingly.

Our experiments are executed on a $7 \times 6 = 42$ qubit patch of 114 qubits within Sqale’s $14 \times 16 = 224$ site array. The qubit array has sufficient spacing between sites to allow qubits to be moved in-between sites; further, the atom motion can be done in parallel. Although we did not explicitly benchmark fidelities during the course of

these experiments, in prior work on a similar Sqale system, we measured up to 99.73(3)% post-selected CZ fidelity (99.35(4)% raw) [16], with median values of 99.48% post-selected (98.8% raw) across nine pairs on a hexagonal lattice [4]. In general, in this paper, we post-select on atom loss, except when performing *loss correction*.

B. Logical Encoding

The realization of high-performance quantum error-correcting (QEC) codes is essential for enabling fault-tolerant quantum computation (FTQC) at scale. Physical qubits are intrinsically fragile, as they are subject to decoherence, gate imperfections, and environmental noise. To mitigate these effects, imperfect physical qubits can be redundantly encoded into logical qubits that achieve significantly higher gate fidelities. The characteristics of QEC codes—such as their encoding rates, resource overhead, and connectivity requirements—vary across code families, making certain codes more suitable than others for specific hardware architectures. In this work, we encode our logical qubits in 2 different codes: the $[[4, 2, 2]]$ code and the $[[16, 4, 4]]$ many-hypercube code. Each circuit is compiled to Sqale’s native gateset [16], which includes state preparation, two-qubit CZ gates, single-qubit global rotation $GR_{\theta, \phi}$ and R_z gates, atom movement, and measurement.

The $[[4, 2, 2]]$ (C_4) code is a Calderbank-Shor-Steane (CSS) stabilizer code that encodes 2 logical qubits within 4 physical qubits. It has a distance of $d = 2$ meaning that a single error can be detected but not corrected. Its stabilizers are $XXXX$ and $ZZZZ$ which admits the following encoding:

$$\begin{aligned} |00\rangle_L &= (|0000\rangle + |1111\rangle) / \sqrt{2} \\ |01\rangle_L &= (|0011\rangle + |1100\rangle) / \sqrt{2} \\ |10\rangle_L &= (|0101\rangle + |1010\rangle) / \sqrt{2} \\ |11\rangle_L &= (|0110\rangle + |1001\rangle) / \sqrt{2} \end{aligned} \quad (1)$$

For this code, the CNOT gate is transversal. The encodings for the fault-tolerant logical gateset, as well as their corresponding compilations to Sqale’s native gateset, can be found in the appendix of our previous work [4]. Compilations for the circuits were performed with the Superstaq [17] optimizing compiler.

The Sqale architecture has implemented the $[[4, 2, 2]]$ code before [4]; however, it was done statically by arranging atoms into a hexagonal lattice to enable a ring connectivity that made it suitable for implementing fault-tolerant encodings. In this paper, the qubits are arranged in a square grid, and we use the motion of flag qubits to achieve ring connectivity.

While only an error detection code, recent work has shown that the $[[4, 2, 2]]$ code can be concatenated with other detection codes to produce high threshold error correction codes with encoding rates 10-100x better than the

surface code [18]. To that end, in Section V, we demonstrate how to prepare a $[[16, 4, 4]]$ many-hypercube code patch [12], as an evolution of the $[[4, 2, 2]]$ code via code concatenation with itself.

C. Post-Processing

Once the measurements are collected from hardware, they are post-processed via (atom) loss-detection, (atom) loss correction, decoding, and/or Pauli-correction.

Loss detection: A result is discarded whenever an atom is not detected at an expected site during measurement.

Loss correction: As an alternative to post-selection on atom loss, we can instead attempt to *correct* for single atom loss events by inferring a state for the lost atom that would complete a logical codeword. For instance, upon reading out $|1112\rangle$, where $|2\rangle$ indicates an atom loss, the decoder can correct to $|1111\rangle$ which corresponds to $|00\rangle_L$. We leave implementation of more sophisticated loss correction decoding that is aware of underlying physical circuits [19–21] to future work.

Decoding: To know if a measurement can be mapped to a logical state, it must first be checked for non-zero flags and out-of-codespace patches. Non-zero measurements of flag qubits indicate that its corresponding patch of data qubits was not correctly initialized into the logical $|00\rangle_L$ state. Any measurement for which not all flags are measured to be zero is discarded. A patch of data qubits is out-of-codespace if it does not match one of the codewords of the $[[4, 2, 2]]$ code (Equation 1). Any measurement for which not all patches are within the codespace is discarded. Once these checks are completed, the remaining measurements are decoded via Equation 1.

Pauli Correction (for constant depth circuits): Appropriate Pauli-corrections (bit-flips) are applied to the data qubit measurements based on the ancilla qubit measurements. This step is the result of pushing the classically-controlled Pauli corrections (that are required to make a circuit constant-depth) past the measurements.

D. Leakage Detection

Non-loss leakage errors occur when the state of a physical qubit escapes the two-level subspace spanned by the prescribed computational basis states $|0\rangle$ and $|1\rangle$. On Sqale, non-loss leakage is predominant on two energy levels which are indistinguishable from the $|0\rangle$ and $|1\rangle$ computational states during readout. Although non-loss leakage can be converted to loss at the hardware level [20, 22], leakage detection units (LDU) detect non-loss leakage without hardware modifications [23, 24]. Logically, each LDU comprises two CNOTs targeting a flag qubit, conditioned on opposite states of the qubit to be

observed:



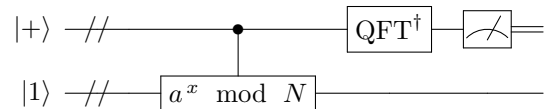
The flag will be $|0\rangle$ if and only if the control qubit is in the qubit subspace because the CX gates have no effect when the control is in a non-loss leaked state.

E. Noisy Simulations

Quantum circuit simulation under realistic noise modeling is fundamental to the design and validation of error-corrected quantum computation, and relies heavily on modeling errors specific to the qubit modality of interest [25, 26]. Our Sqalesim simulator [4] models each atom as a five-level system composed of the computational basis qubit subspace $\{|0\rangle, |1\rangle\}$, two leakage states, and a loss state. Whereas the previous implementation of Sqalesim [4] relied primarily on density matrix simulation, the current implementation achieves greater efficiency by simulating operations that only affect the qubit subspace through a Clifford-only simulator. Any non-Clifford operation is replaced with its Pauli Twirling approximation. Transitions in and out of the qubit subspace are tracked using a classical distribution that describes the probability of the atom being in each non-computational state. The current implementation also models atom motion, where each atom being moved has a probability that its qubit subspace undergoes a phase error.

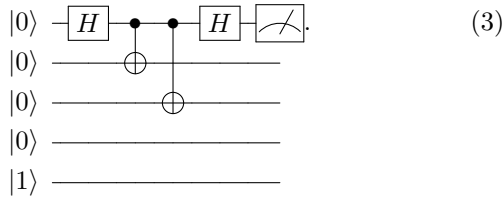
III. SHOR'S ALGORITHM (PRE-COMPILED)

The heart of Shor's Algorithm [27] is the quantum order-finding subroutine, which determines the period r such that $a^r \equiv 1 \pmod{N}$ for a given base a and semiprime integer N to be factored. The order-finding algorithm in turn comprises the following circuit:



In this circuit (where $//$ denotes a bundle of quantum wires), the top register is initialized to the uniform superposition ($|+\rangle$) state and acts as the control for the modular exponentiation. The bottom register is initialized to $|1\rangle$ and undergoes the modular multiplication operation $a^x \bmod N$, where the exponent x is determined by the state of the control register. Following modular exponentiation, the inverse Quantum Fourier Transform (QFT) is applied to the control register, which enables extraction of the period, r , after final measurement. Information about r is then classically processed via the continued fractions algorithm, allowing deduction of the factors of N .

In general, the base a is to be chosen randomly. However, there exist choices such that $a^{2^k} \equiv 1 \pmod{N}$ for some k , causing the sequence to terminate and the circuit to be smaller. It is known that such an a always exists for $k = 1$ [11], at which point the circuit reduces to a Hadamard test with a single controlled-modular multiplier. The multiplier itself has a known input and can therefore be replaced with a few CNOTs. Such pre-compiled constructions are inherently unscalable because they depend on prior knowledge that is effectively equivalent to knowing the answer in advance. A truly scalable version of Shor's Algorithm instead coherently executes the modular arithmetic on the quantum computer itself, without access to this hidden information. As a result, the complexity of the order-finding algorithm can be significantly reduced with special values of the base a for modular exponentiation. For $N = 15$, the choices are $a \in \{4, 11, 14\}$. Taking $a = 11$ for $N = 15$, the pre-compiled order-finding circuit is simply:

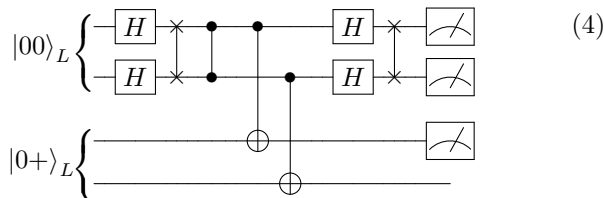


For our experiments we drop the two unused qubits, leaving just the three-qubit Hadamard test circuit. We refer to the Sqale compiled version of this as the ‘unencoded Shor’ circuit.

Though the order-finding algorithm only requires measurements from the top (QFT register) qubit, we validate our experiments by measuring all three non-idle qubits and compare the resulting distribution to that of the ideal distribution using the metric of Total Variation Distance (TVD).

A. Logical circuits

Two embeddings, called two-row Shor and three-row Shor of the unencoded Shor circuit, are encoded in logical $[[4, 2, 2]]$ qubits, using only the code's fault-tolerant state preparation and transversal operations [4]. Two-row Shor requires two logical patches, but makes use of three of the four resulting logical qubits:

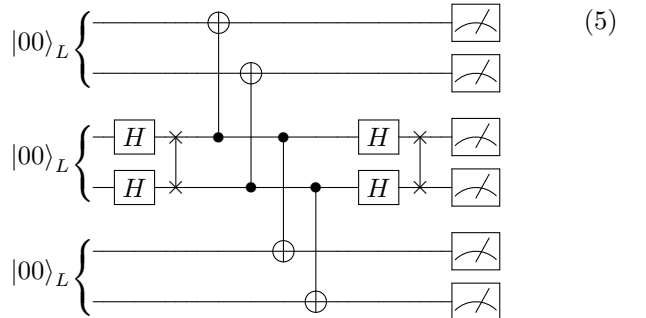


The two registers are arranged linearly in adjacent rows, ensuring that the transversal CX gates are all performed between neighboring qubits. The lower patch is initialized in the $|0+\rangle_L$ state, so the CX gate has no effect on

the (unused) $|+\rangle$ qubit. The remaining operations are then equivalent to those in Equation 3 on the three $|0\rangle$ -initialized logical qubits. The preparation of $|00\rangle_L$ in the upper register requires a flag qubit and ring connectivity, as described in Section II. We achieve the necessary connectivity via a single atom move, transporting the flag qubit from one end of the patch to the other to allow CNOTs from the data qubits on either side. The circuit is compiled to the Sqale native gateset, and the final compiled circuit contains 11 CZ gates, 5 GR gates, and one movement operation.

The two-row Shor experiment is also repeated with LDUs on the eight data qubits near the end of the circuit before the final round of Hadamards in Equation 4. This allows for a more efficient compilation than if they were placed at the end of the circuits. This compilation procedure is justified because subsequent operations are not expected to contribute substantially to leakage errors. In postprocessing, a nonzero measurement of any LDU flag qubit is treated identically to an observed atom loss on the corresponding data qubit. These flag qubits are placed in additional rows of atoms above and below the two logical patches. In total, the addition of LDUs requires an additional 16 CZ gates and one GR.

Three-row Shor uses three logical patches, but avoids the wasted logical qubit in the two-patch variant. Instead, the three-qubit circuit is implemented transversally across the three registers, so that in effect it is replicated for each logical qubit in each register:



As a result, each run of the encoded circuit generates two independent samples of the circuit.

Like the two-row Shor, logical patches are stacked on adjacent rows of atoms to allow transversal CNOTs between adjacent patches. In this case all three patches are initialized to $|00\rangle_L$, requiring their own flag qubits. The three flags are initially placed in a single column on one side of the logical patches, and are simultaneously transported to the other end of their respective registers in a single motion operation.

Three-row Shor's requires twice as many CZs (22) but the same number GRs (5) as the two-row Shor when compiled to the Sqale gateset.

B. Results

Experimental results from four implementations: unencoded, two-row logical encoding, three-row logical encoding, and two-row with leakage detection, as well as those predicted via noisy simulation, are displayed in Fig. 2. All results are post-selected on atom loss (see Section IX D for results with loss correction post-processing instead). The three encoded implementations are additionally post-selected on flag qubits for their $|00\rangle_L$ preparation and the parity of the measured data qubits, as well as (in the case of the leakage-detecting circuit) the measured state of the eight LDU flags. At least 5×10^3 shots were taken per circuit, with 10^4 shots of the leakage detection circuit to compensate for its low post-selection yield.

We see statistically significant drops in TVDs between the unencoded and each of the encoded circuits. Notably, despite getting two samples per shot, we find that after the same number of shots, the three-row logical circuit has substantially fewer valid samples after post-selection than the two-row variant (1152 vs. 1986). At the same time, we see a discernible drop in TVD between the two-row embedding to the three-row embedding, more so than initially predicted by their noisy simulation (investigated further in Section IX A 1). Though they resulted in a substantially lower post-selection yield, we did not see an advantage (in terms of TVD) from using the leakage detection units (LDU). We attribute this to the considerable noise added from the additional two-qubit gates, and expect that the same units would prove beneficial within a deeper circuit in which the leakage is more likely to have occurred. Indeed, we do see a substantial increase in TVD (from 6.7% shown to 14.1%) if we reinterpret the same results without post-selecting on the LDU flags.

IV. CONSTANT-DEPTH CNOT-LADDERS

A CNOT-ladder is a series of CNOT (controlled-NOT) gates used to compute the binary sum (mod 2) of a set of qubits' states [14]. CNOT-ladders are a crucial sub-component of many fundamental circuits in quantum computing including modular exponentiation for Shor's algorithm [27], GHZ-state preparation, and Pauli-phasors for Hamiltonian simulation.

Because addition is both commutative and associative, the CNOT-ladder may be arranged in any manner that achieves this summation. As we wish to ultimately encode a CNOT-ladder via the $[[4, 2, 2]]$ code on a nearest-neighbor architecture, we consider the “outside-in” CNOT-ladder arrangement, a 5-CNOT example of which is shown in Figure 3a. It only requires linear nearest-neighbor connectivity but note that it can be embedded into a 2×3 grid. This is shown via the double-indexed qubit labels after the arrows.

Figure 3b shows the same circuit as Figure 3a but with the double-indexed qubit labels rearranged to place the

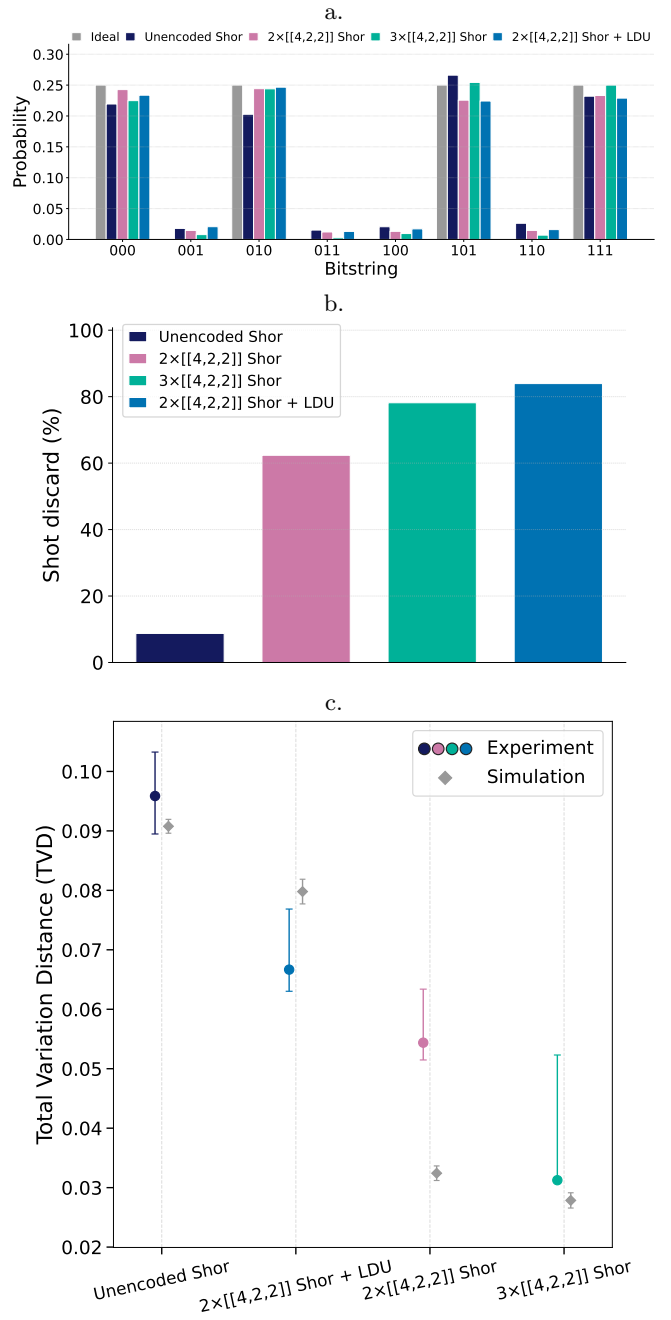
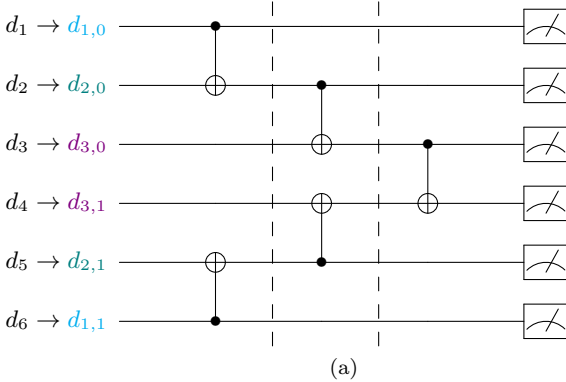
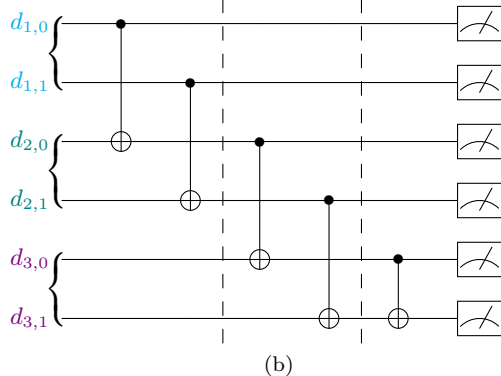


FIG. 2. Experimental results for all Shor circuits run on hardware. (a) The measured probability distribution, (b) The post-selection discard, and (c) The TVD computed between the experimental and ideal distributions in (a). The error bars represent a 68% confidence interval (CI) on the TVD for the narrowest CI obtained through minimization of the CI width. Diamond data points represent the expected (mean) TVD from a default Sqalesim noise sampling for the same number of experimental shots, with error bars on the mean of ten trials.



(a)



(b)

FIG. 3. An “outside-in” implementation of a CNOT-ladder consisting of 5 CNOTs. Sub-figure (a) shows an implementation on a 6×1 line (or 3×2 grid) of qubits with nearest-neighbor connectivity. Sub-figure (b) is a rearrangement of (a) via row-major ordering. The CNOT-ladder places the sum (modulo 2) of every individual qubits’ state on the middle/last qubit for sub-figures (a)/(b) respectively. The dashed barriers delineate segments of the circuit that can be executed in parallel and the brackets denote qubits within the same row.

qubits within the same row next to one another. One should think of this arrangement as two initial CNOT-ladders being executed on the two columns of qubits in parallel followed by a single CNOT that adds their respective partial summations. Furthermore, and most importantly, this arrangement allows for a convenient logical encoding in which each row of qubits are designated to be the two logical qubits within a $[[4, 2, 2]]$ patch. With this encoding, each CNOT simply acts transversely between patches (except for the last one, which acts within the final patch).

A. To Constant-Depth

In this experiment, we run circuits that allow CNOT-ladders to be executed in constant depth. More generally, there exists a space-time tradeoff for quantum circuits that enables one to employ entanglement, mid-circuit measurement, and feed-forward operations to reduce circuit-depth at the expense of requiring additional

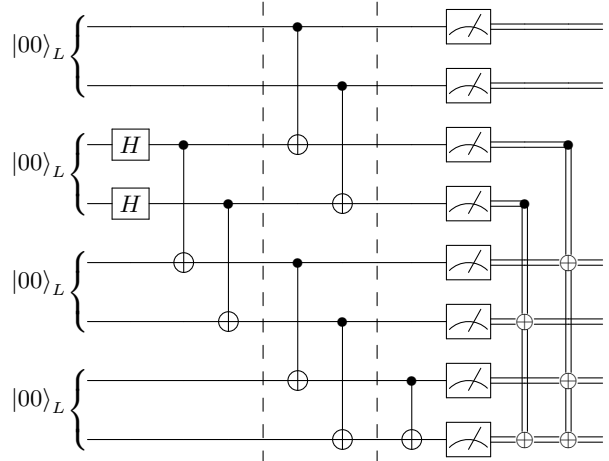


FIG. 4. Logical circuit for a 5 CNOT, constant-depth CNOT-ladder on a 4×2 grid of qubits. The brackets surround qubits on the same row. The dashed lines separate the circuit into three parts: the first creates a Bell pair between the ancilla row and the second data row, the second consists of the CNOTs from the first two sections of the original circuit (Figure 3b) being executed in parallel, and the third consists of the final CNOT from the original circuit, measurement, and classical correction.

qubits [14, 28, 29]. This exchange can be quite favorable since decreasing the depth of a quantum circuit decreases the noise it suffers due to depolarization [30], and is particularly well-suited to neutral atom architectures that can support many thousands of qubits within a single trap [31].

To illustrate the reduction of a CNOT-ladder to constant depth, we start with a small example: the 6-qubit ladder shown in Figure 3b. We will reduce its depth by parallelizing its first two sections (where sections are delineated by dashed vertical lines), ultimately resulting in the circuit shown in Figure 4. This can be achieved by introducing a row of two ancilla qubits between the first two rows of data qubits. This ancilla row is then pairwise entangled with the second data row by preparing them in a GHZ state: $(|0000\rangle + |1111\rangle)/\sqrt{2}$. Because of this entanglement, it is as if the targets of the first CNOT pair (of the second section of Figure 4) were applied not on the ancilla row, but the second data row, before the targets of the second CNOT pair. The catch is that this is only true if the ancilla row is measured to be $|00\rangle$. If it is not, one could imagine that it would have been had the appropriate set of X gates been applied immediately before measurement. For this circuit, these “correcting” gates can be pushed down the circuit and past the measurement where they can be implemented as bit-flips in post-processing. The four rows of logical qubits are initialized to the logical $|00\rangle_L$ state of the $[[4, 2, 2]]$ code (Equation 1). Each of these initializations requires a fifth physical qubit acting as a flag qubit to ensure the fault-tolerance of the preparation. To achieve

the ring connectivity required for this preparation, the entire column of flag-qubit atoms is moved, mid-circuit, from the last column of the trap array to the first, as depicted in the upper panel of Figure 1c(ii). This circuit (Figure 4) is shown at the logical level but may be decomposed to the physical level via the $[[4, 2, 2]]$ code (and further to Sqale’s native gate-set) via the decomposition found in the appendix of our previous work [4].

This logic may be extended to arbitrarily long CNOT-ladders as shown in Figure 15 of Appendix IX C. In particular, the logical circuit for the 12 logical qubit experiment is simply this figure without the ellipses. In this generalization, the post-processing is as follows: the measured bit of a data qubit is flipped if the measured bit-string of the previous ancilla qubits (along the same column) has even parity (except for the last data qubit for which the bit-string of all previous ancilla qubits is considered)

Here we can achieve this logical, constant-depth scaling due to the use of $[[4, 2, 2]]$ patches where each patch sits in a row of atoms, as shown in Figure 1. Movement costs are constant, as transversal CNOTs require no movement and flag qubits only move a fixed horizontal distance. Going forward, however, we will be interested in performing such circuits on logical qubits of arbitrary distance d , where each code block may require a 2D array of atoms whose width and height scale with d . When performing transversal CNOTs or state preparation, movement time will therefore also scale with d . While this may suggest the loss of a constant-depth advantage (as we will discuss in Section VI A) the logical, nearest-neighbor circuit structure keeps movement times short, allowing the dominant time cost of gate layers to remain constant for relevant code distances.

B. Results

We collected experimental results for both unencoded and encoded constant-depth CNOT ladders with both 8 and 12 logical qubits. The measurements of these circuits are post-processed via loss detection, decoding (for the encoded circuits), and Pauli-correction (as described in Section II C). The unencoded and encoded 8 logical qubit circuits had a post-processing survival rate of 0.804 and 0.066, respectively. Meanwhile, the unencoded and encoded 12 logical qubit circuits had a post-processing survival rate of 0.768 and 0.009, respectively. Here we report error rates: the fraction of post-processed measurements equal to the single, expected bit-string for each ladder. The results for the 8 logical qubit experiment are given in Figure 5. For this experiment, we collected data over 10 random initial product states. We note that every encoded circuit achieves a statistically significant decrease in error rate compared to its unencoded counterpart. On average the encoded error rate is nearly 4 times lower than the unencoded error rate. The results for the 12 logical qubit experiment are given in Figure 6. For this

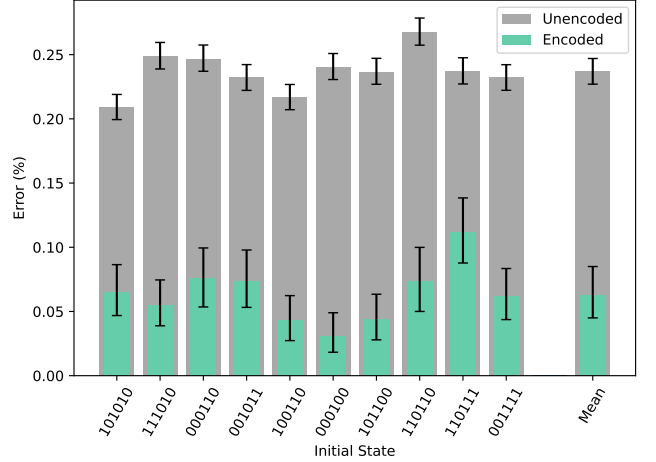


FIG. 5. Error rates with 68% confidence intervals for unencoded (gray) vs encoded (green) constant-depth CNOT ladders with 8 logical qubits. The mean unencoded and encoded error rates are 0.237 (0.227, 0.247) and 0.063 (0.045, 0.085), respectively.

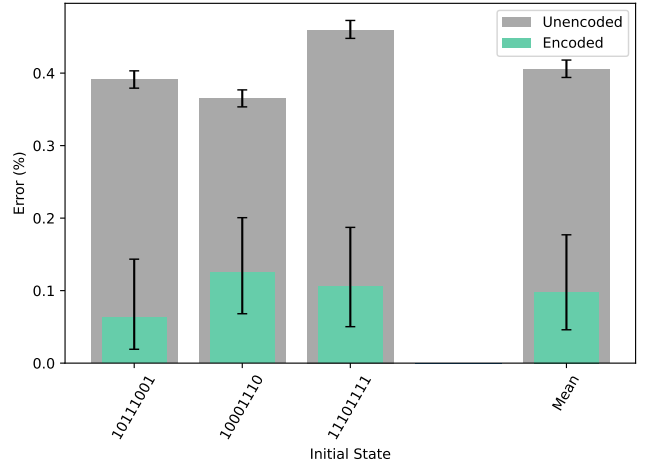


FIG. 6. Error rates with 68% confidence intervals for unencoded (gray) vs encoded (green) constant-depth CNOT ladders with 12 logical-qubits. The mean unencoded and encoded error rates are 0.405 (0.393, 0.417) and 0.098 (0.046, 0.177), respectively.

experiment, we collected data over 3 random initial product states. On average the encoded error rate is over 4 times lower than the unencoded error rate. We note that although the absolute error rates increased when increasing logical qubit count from 8 to 12, the improvement factor remained roughly the same, suggesting that said improvement may be maintained with further increases to logical qubit count.

V. MANY-HYPERCUBE CODE

We can recursively concatenate the $[[4, 2, 2]]$ code introduced in Section II B with itself to obtain a family of high-rate and high threshold codes known as many-hypercube codes [12].

In this section we demonstrate the initialization of a $L = 2$ many-hypercube code derived from concatenating the $[[4, 2, 2]]$ code with itself once.

We first write the stabilizers for the $[[4, 2, 2]]$ code as

$$S_X^{(1)} = [X \ X \ X \ X], \quad S_Z^{(1)} = [Z \ Z \ Z \ Z],$$

and in a similar way write the logical operators as

$$\begin{aligned} \bar{X}_1^{(1)} &= [I \ X \ X \ I], & \bar{Z}_1^{(1)} &= [Z \ I \ Z \ I], \\ \bar{X}_2^{(1)} &= [I \ X \ I \ X], & \bar{Z}_2^{(1)} &= [Z \ I \ I \ Z]. \end{aligned}$$

We can then write the six X and Z stabilizers for the $[[16, 4, 4]]$, $L = 2$ many-hypercube code as:

$$S_X^{(2)} = \begin{bmatrix} S_X^{(1)} & I & I & I \\ I & S_X^{(1)} & I & I \\ I & I & S_X^{(1)} & I \\ I & I & I & S_X^{(1)} \\ \bar{X}_1^{(1)} & \bar{X}_1^{(1)} & \bar{X}_1^{(1)} & \bar{X}_1^{(1)} \\ \bar{X}_2^{(1)} & \bar{X}_2^{(1)} & \bar{X}_2^{(1)} & \bar{X}_2^{(1)} \end{bmatrix},$$

$$S_Z^{(2)} = \begin{bmatrix} S_Z^{(1)} & I & I & I \\ I & S_Z^{(1)} & I & I \\ I & I & S_Z^{(1)} & I \\ I & I & I & S_Z^{(1)} \\ \bar{Z}_1^{(1)} & \bar{Z}_1^{(1)} & \bar{Z}_1^{(1)} & \bar{Z}_1^{(1)} \\ \bar{Z}_2^{(1)} & \bar{Z}_2^{(1)} & \bar{Z}_2^{(1)} & \bar{Z}_2^{(1)} \end{bmatrix},$$

and the logical operators as:

$$\begin{aligned} \bar{X}_1^{(2)} &= [I \ \bar{X}_1^{(1)} \ \bar{X}_1^{(1)} \ I], & \bar{Z}_1^{(2)} &= [\bar{Z}_1^{(1)} \ I \ \bar{Z}_1^{(1)} \ I], \\ \bar{X}_2^{(2)} &= [I \ \bar{X}_1^{(1)} \ I \ \bar{X}_1^{(1)}], & \bar{Z}_2^{(2)} &= [\bar{Z}_1^{(1)} \ I \ I \ \bar{Z}_1^{(1)}], \\ \bar{X}_3^{(2)} &= [I \ \bar{X}_2^{(1)} \ \bar{X}_2^{(1)} \ I], & \bar{Z}_3^{(2)} &= [\bar{Z}_2^{(1)} \ I \ \bar{Z}_2^{(1)} \ I], \\ \bar{X}_4^{(2)} &= [I \ \bar{X}_2^{(1)} \ I \ \bar{X}_2^{(1)}], & \bar{Z}_4^{(2)} &= [\bar{Z}_2^{(1)} \ I \ I \ \bar{Z}_2^{(1)}]. \end{aligned}$$

We verify this indeed corresponds to a code distance $d = 4$ through a brute-force search using the qLDPC library from Infleqton and open-source collaborators [32].

A. Logical Circuits

To concatenate the $[[4, 2, 2]]$ code with itself, we prepare five $[[4, 2, 2]]$ logical patches in the $|00\rangle$ state, where each patch is a row of four data qubits and an additional flag qubit. We move the last column of flag qubits to

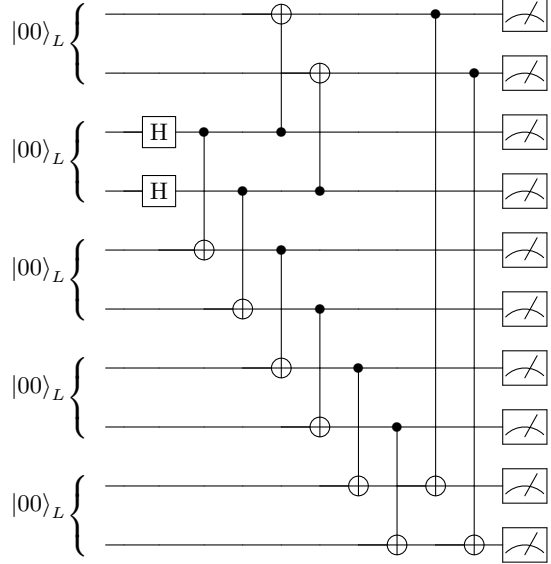


FIG. 7. $L = 2$ Many-hypercube state preparation circuit. The five pairs of qubits are initialized to the logical $|00\rangle_L$ state of the $[[4, 2, 2]]$ code (Equation 1).

complete the fault-tolerant state preparation routine. We now perform the same state preparation circuit, but on our logical patches, where the first four patches become logical data qubits and the fifth patch becomes a logical flag qubit. This requires moving the logical flag qubit row, as described in Fig. 1c(i). We now have a $|0000\rangle$ state in the $[[16, 4, 4]]$ code. To prepare specific states, we apply transversal X gates to the relevant qubits. Descriptions of the relevant fault-tolerant state preparation and transversal operations can be found in [4].

B. Results

We collected experimental results for unencoded and encoded ($[[16, 4, 4]]$) state preparation of the following bitstrings – “1110”, “0000”, “0111”, and “1111”. The measurements of these circuits are post-processed via loss detection and decoding (for the encoded circuits). Stabilizer values are reconstructed from data qubit measurements at the end of the circuit. As a result, only Z stabilizers are used for decoding. Across all bitstrings, the encoded circuits have a lower error rate than the unencoded ones. On average, we get an encoded error rate of 0.0421, a significant performance gain on the 0.1721 unencoded error rate (although, there is some expected system drift based on simulation predictions seen in Section IX B). We also compute a mean error rate by collecting all of the correct and incorrect counts across the four bitstrings and comparing them to the ideal case (where all the counts correspond to the correct bitstring). The mean post-

selection rate for the encoded circuits is 5.63%, while the unencoded circuits have no atom loss events. The full result can be seen in Figure 8.

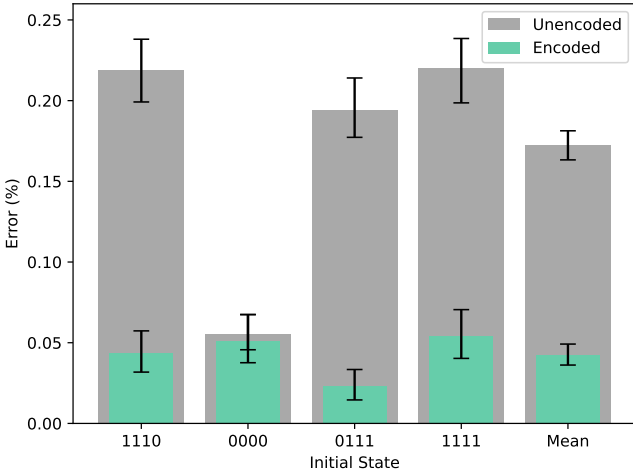


FIG. 8. Experimental demonstration of the many-hypercube state preparation for various initial states. The plot compares error rate (with error bars for a 68% confidence interval) for unencoded (gray) vs. encoded (green) state preparation for an assortment of bitstrings.

VI. OUTLOOK

A. Towards a Constant-Depth Architecture

For platforms such as neutral atoms where space-time trade-offs favor reduced time costs, an appealing target is a constant-depth, logical architecture [33]. Three hardware upgrades will be needed to realize a constant-depth architecture on Sqale: Parallel gates, mid-circuit measurements, and a more scalable tuning system. We now motivate how the experimental demonstrations in this work fit into a logical architecture for constant-depth circuits at scale. Importantly, two mechanisms that were demonstrated – atom movement and syndrome decoding – in addition to two that weren’t as of yet – parallel gates and mid-circuit measurements – will scale with the code distance d . Here, we discuss how our focus on logical constant-depth circuits allows these mechanisms to avoid increasing logical circuit depth due to manageable constant factors.

1. Movement Operations

For general CSS codes of arbitrary distance d , we can implement constant-depth logical circuits using transversal CNOTs and atom movement. However depending on how much atom movement is needed, a logical gate layer can be *measurement-bottlenecked* or *movement-bottlenecked*. We argue that for any relevant code

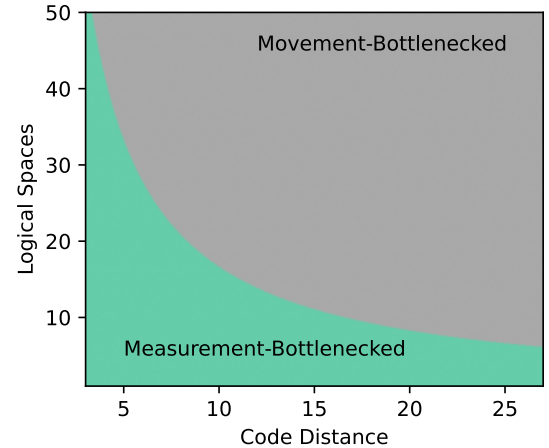


FIG. 9. Dominant time cost of a gate layer involving a transversal CNOT via movement for varying values of code distance and logical movement spaces.

distance, the logical circuits we target will always be measurement-bottlenecked.

Figure 9 shows two operational regimes bottlenecked by measurement and movement, respectively, demonstrating which dominates gate layer cost for varying code distance and logical movement. The analysis assumes a logical movement space corresponds to moving d physical spaces, such as with the surface code. Measurement is assumed to take 1 ms. Since all of the circuits we consider in this work require short, constant logical movements, the number of logical spaces per CNOT remains small, and in most cases is only 1. For all relevant code distances, this corresponds to gate layers where measurement is the dominant time cost, not movement.

2. Syndrome Decoding

Code deformation techniques for performing logic [34–36] require a number of syndrome measurement rounds scaling as $O(d)$ to handle measurement errors properly. In contrast, transversal gates can require $O(1)$ syndrome measurement rounds so long as proper decoding techniques are used [37, 38]. These decoding techniques, however, require a decoding volume scaling with the number of logical qubits included in the *observing region* for an $O(d)$ round decoding window. For a worst-case circuit, such as a depth- $O(d)$ tree of CNOTs, the observing region can contain $2^{O(d)}$ logical qubits. In such a case, stalls from decoding complexity can erase a constant-depth advantage. In contrast, our architecture only uses constant, near-neighbor logical movement operations for multi-qubit logical operations. The number of logical qubits that can be in the observing region after $O(d)$ rounds is therefore at most $O(d^2)$, allowing us to avoid scaling slowdowns from decoding. Furthermore, longer cycle times present in neutral atoms gives additional

headroom to avoid constant factor effects in decoding overhead.

VII. CONCLUSION

This work presents a neutral atom quantum computing architecture that unites qubit motion with individual optical addressing to run logical quantum circuits. This architecture addresses the overhead of excessive atom motion that might ultimately hamper the scaling of utility-scale quantum computers [9]. The experimental demonstrations exhibit improved logical-over-physical performance for the first demonstrations of logical pre-compiled Shor circuits and logical constant-depth circuits.

Two complementary ingredients underpin these results. First, compiler-level transformations recast the logical circuits into a constant-depth format that optimizes qubit placement to minimize movement overhead. Second, in-place operations enable fast and more accurate entanglement without requiring movement before every gate, mitigating a dominant contributor to wall-clock runtime and error accumulation. Together, these features enable a neutral atom architecture that seeks to minimize circuit depth and runtime at the expense of increased qubit count: a trade-off well matched to neutral atom systems, which can increase qubit number within a single glass cell more readily than they can accelerate native gate times.

Looking ahead, the current single-species implementation described in this work would still require motion for mid-circuit measurements; extending to dual-species arrays (or even hiding beams) would enable in-place readout and further reduce both runtime and error [39, 40]. Continued development of motion-aware, logic-to-device compilers will be central to exploiting constant-depth paradigms at larger scale. By consolidating recent hardware and compilation advances, the architecture presented lays the groundwork for further increases in scale towards large, fault-tolerant quantum computers.

VIII. ACKNOWLEDGEMENTS

We thank Cord Mazzetti, Sayam Sethi, and Jonathan Mark Baker for their discussions regarding early fault-tolerant implementations of Shor’s algorithm.

This material is based upon work supported by the U.S. Department of Energy, Office of Science, Office of Advanced Scientific Computing Research, under Award Numbers DE-SC0021526 and DE-SC0025493. Work on this manuscript is supported by Wellcome Leap as part of the ‘Quantum Biomarker Algorithms for Multimodal Cancer Data’ research project within the Quantum for Bio (Q4Bio) Program. This work is also funded in part by the STAQ project under award NSF Phy-232580; in part by the US Department of Energy Office of Advanced Scientific Computing Research, Accelerated Research for

Quantum Computing Program; and in part by the NSF Quantum Leap Challenge Institute for Hybrid Quantum Architectures and Networks (NSF Award 2016136). This work was completed in part with resources provided by the University of Chicago’s Research Computing Center.

Disclaimer: This report was prepared as an account of work sponsored by an agency of the United States Government. Neither the United States Government nor any agency thereof, nor any of their employees, makes any warranty, express or implied, or assumes any legal liability or responsibility for the accuracy, completeness, or usefulness of any information, apparatus, product, or process disclosed, or represents that its use would not infringe privately owned rights. Reference herein to any specific commercial product, process, or service by trade name, trademark, manufacturer, or otherwise does not necessarily constitute or imply its endorsement, recommendation, or favoring by the United States Government or any agency thereof. The views and opinions of authors expressed herein do not necessarily state or reflect those of the United States Government or any agency thereof.

FTC is an advisor to Quantum Circuits, Inc.

Infleqtion and Collaborators

Rich Rines^{1,‡}, Benjamin Hall^{1,‡}, Mariesa H. Teo^{4,‡}, Joshua Viszlai^{1,3,‡}, Daniel C. Cole^{1,‡}, David Mason^{1,‡}, Cameron Barker¹, Matt J. Bedalov¹, Matt Blakely¹, Tobias Bothwell¹, Caitlin Carnahan¹, Frederic T. Chong^{1,3}, Samuel Y. Eubanks¹, Brian Fields¹, Matthew Gillette¹, Palash Goiporia¹, Pranav Gokhale¹, Garrett T. Hickman¹, Marin Iliev¹, Eric B. Jones¹, Ryan A. Jones¹, Kevin W. Kuper¹, Stephanie Lee¹, Martin T. Lichtman¹, Kevin Loeffler¹, Nate Mackintosh¹, Farhad Majdeteimouri¹, Peter T. Mitchell¹, Thomas W. Noel¹, Ely Novakoski¹, Victory Omole¹, David Owusu-Antwi¹, Alexander G. Radnaev¹, Anthony Reiter¹, Mark Saffman^{1,2}, Bharath Thotakura¹, Teague Tomesh¹, Ilya Vinogradov¹.

¹ Infleqtion (Boulder, CO, USA; Chicago, IL, USA; Louisville, CO, USA; Madison, WI, USA; Oxford, England, UK)

² Department of Physics, University of Wisconsin-Madison, Madison, WI, USA

³ Department of Computer Science, University of Chicago, Chicago, IL, USA

⁴ Pritzker School of Molecular Engineering, University of Chicago, Chicago, IL, USA

[‡] These authors contributed equally to this work.

IX. APPENDIX

A. Error Factor Simulations

1. *Shor*

We investigated the impact and sensitivity of hardware noise further for the circuits in section III by employing noise scaling analysis to discover their pseudo-thresholding behavior (see Fig. 10). We identified the error sources in Sqalesim most likely to have higher hardware drift and scaled them by a multiplicative factor α (where the default settings correspond to $\alpha = 1$). In taking 5×10^4 raw noisy shots to approximate the infinite shot limit, we observed that the $[[4, 2, 2]]$ encoded Shor circuits maintain a lower TVD compared to the unencoded Shor for all simulated values up to $\alpha = 3.5$ and $\alpha = 4$ for two- and three-row encodings, respectively. It is also interesting to see that there is a clear TVD separation between the two- and three-row Shor circuits themselves (as also observed experimentally in Fig. 2) for all α we simulated above ~ 0.5 . We attribute this general resilience to the strong noise robustness of the $[[4, 2, 2]]$ code for early fault-tolerant circuits [4], with the longer sustained performance of the three-row arising from more opportunities for error detection filtering (additionally seen in Fig. 10 from the higher post-selection discard at higher α for the same number of shots). This highlights that different logical encodings of the same underlying code can exhibit observable differences in the presence of realistic noise, and that a curious balance exists between a compact encoding and seeming distributed logical redundancy. At the same time, we also notice the potential limitations of the $[[4, 2, 2]]$ code with the simulations of the two-row Shor circuit equipped with LDU. Its ‘pseudothreshold’ (that is, the point at which the base unencoded circuit performs better) is drastically lower than its non-LDU standalone and predicts worse performance just after $\alpha \sim 1.1$. We explain this behavior as a predicament in applying numerous CZ gates for the LDU while a dominant CZ error accumulates (along with a proportional atom loss) with increasing α . In particular, being just a distance 2 code, the increasing errors can very

quickly pile up as logical errors, and whatever detection capability is offered by the LDU gets drowned. We note that this is particularly exemplified for the Shor circuits as the order of magnitude of CZs added from the LDU encroaches on the CZ depth of the base encoded circuit itself. Although the LDU is not without its merit in offering better performance than the unencoded Shor in the error regime $\alpha \leq 1$, it signals an informed weighting of importance on the kinds of fault-tolerance gadgets to leverage for a given circuit based on the dominant hardware error sources at play.

2. *Constant-depth CNOT ladder*

We study the simulated performance of constant-depth CNOT (CDCX) ladder circuits as we scale the noise parameters by a constant factor from $0.1 \times$ to $10 \times$. Due to the number of shots required ($> 5 \times 10^5$ for higher scaling factors), these simulations reflect results for a specific initial bitstring for each CDCX size – initial simulations of multiple bitstrings saw little variation in results, giving us reason to believe that the analysis here should hold qualitatively across all initial bitstrings.

Fig. 11 shows the simulated TVDs of the encoded and unencoded circuits for 8 LQ and 12 LQ CDCX circuits. As the simulated noise parameters are scaled up, the encoded circuit outperforms (has a lower TVD than) the unencoded circuit for scaling factors up to about $9 \times$, after which the unencoded circuit has a slightly higher TVD than the encoded circuit. We refer to this crossing point as the pseudothreshold – the error factor below which the encoded circuit outperforms the unencoded circuit.

For comparison, we also mark the average TVDs found for these circuits in experiment. We observe that these results intersect with the simulated curves between $1-2 \times$ the estimated system noise model. The variation of the points of intersection in this range is reflective of variation in the noise present in the physical device over time, and suggests that our estimates of the noise mechanisms and parameters accurately characterize the hardware’s actual performance on average.

As noise is scaled, the proportion of shots thrown out

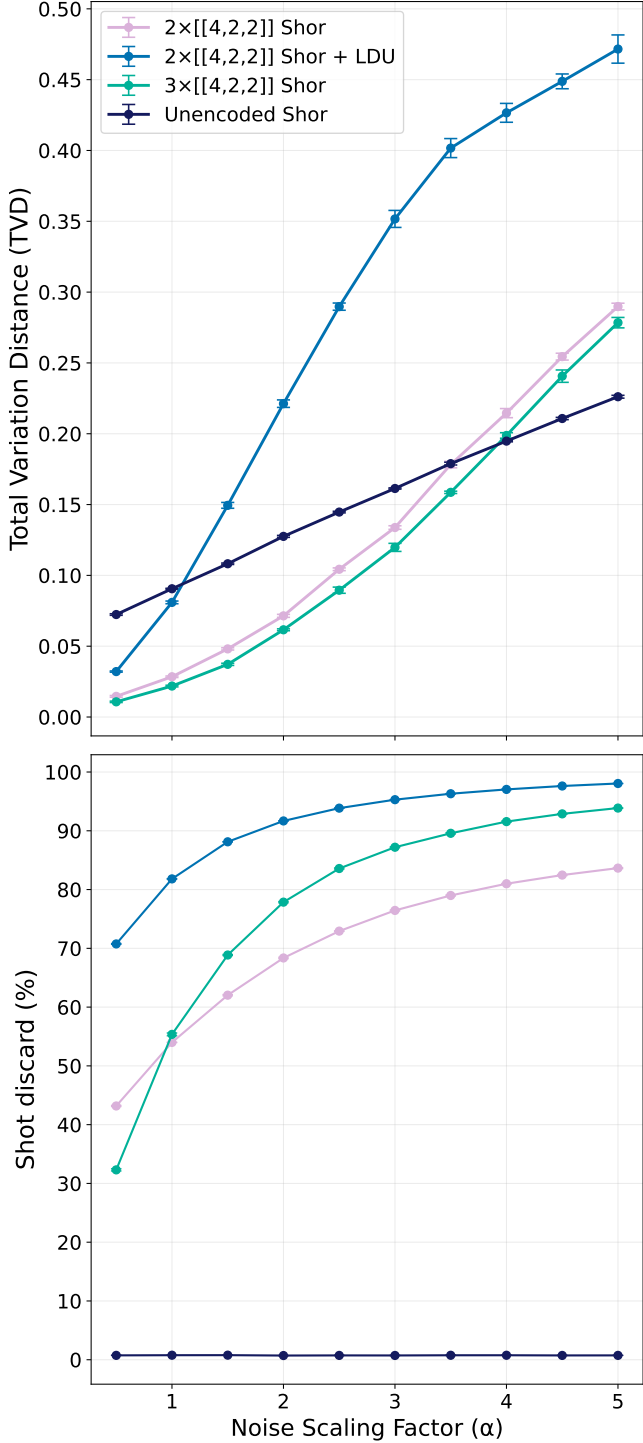


FIG. 10. Noisy simulation results for all executed Shor circuits using Sqalesim. A subset of dominant errors are scaled by a factor α as a proxy for extrapolated noise scaling on hardware. The top plot shows the simulated TVD computed against the ideal distribution, and the bottom plot shows the corresponding shot discard percentage after post-selection. Each data point is the mean value across five repeated trials, with each trial using 5×10^4 shots for a given α . Error bars shown are the standard error of the mean.

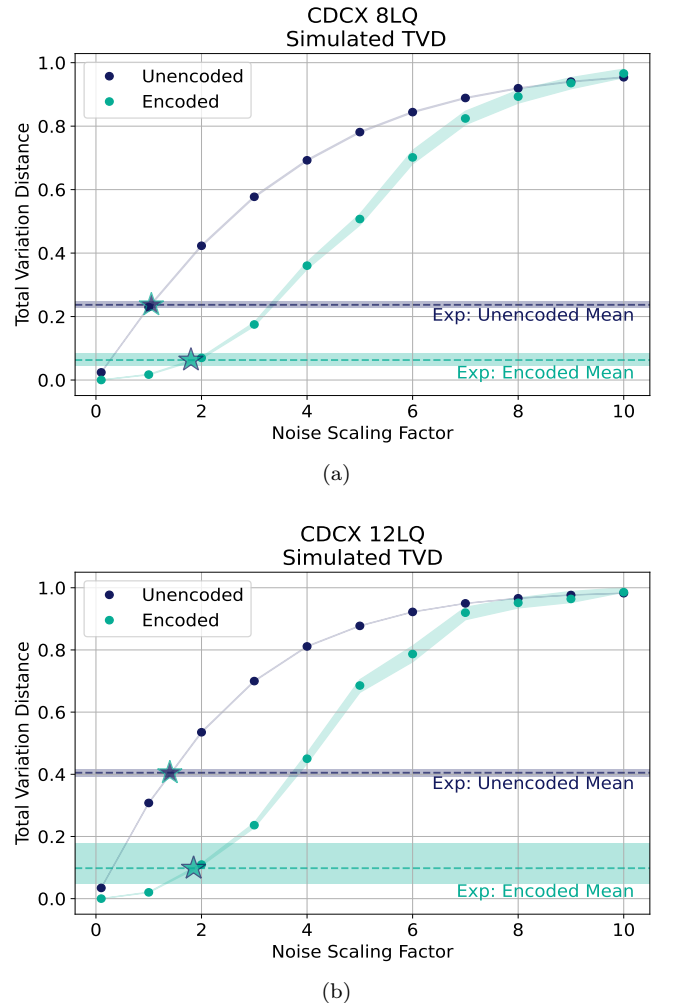


FIG. 11. Simulations of 8 LQ and 12 LQ CDCX circuits while scaling all noise parameters. For comparison, the mean TVDs found in experiment are shown using dashed horizontal lines, with the surrounding shaded area representing the confidence interval. In both cases, their intersections with the simulated curves are marked by stars that lie between 1-2x Error Factor on the x-axis, suggesting that the hardware is, on average, well-characterized by our noise model and estimated noise parameters.

during post-selection also increases. In Fig. 12, we separate the shots discarded from the 8 LQ CDCX circuits into three categories: (1) discarded because a flag qubit flagged an error in the state preparation step, (2) discarded because of loss detection, (3) discarded because the measured output state was not in the codespace. In all cases, the majority of shots are discarded because an error was flagged during the state preparation step.

Finally, we study performance as the number of logical qubits (N) in the CDCX circuits is increased, characterizing performance using two metrics – the estimated pseudothreshold and the proportion of shots discarded (Fig. 13). For each N , we find the range of noise scaling factors where the confidence intervals of the encoded and

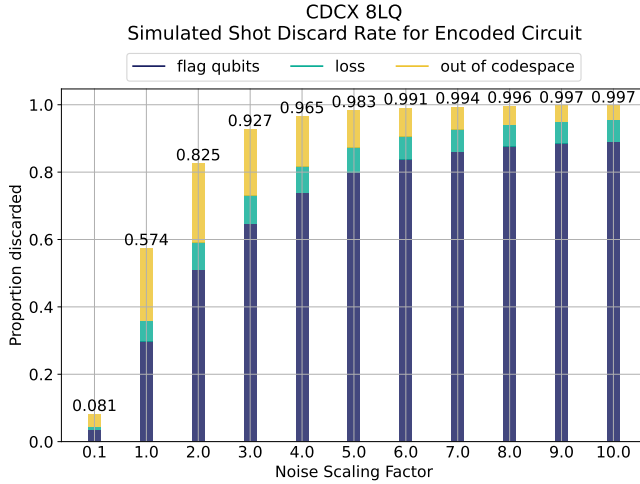


FIG. 12. Simulated proportion of shots discarded for 8 LQ CDCX circuit while scaling all noise parameters. The majority of shots are discarded on account of the flag qubit from the state preparation step, and the remaining are discarded due to loss or being outside the codespace.

unencoded TVDs intersect— this is marked as the pseudothreshold range. We also highlight the proportion of shots that would be discarded at $1\times$ the system error model, to give an idea of the shot budget needed with current device capabilities. As N increases, we observe a decreasing trend in the estimated pseudothreshold, and an increasing trend in the proportion of shots discarded. Our results suggest that at larger system sizes, the physical error rates needed to see the benefits of encoding will be smaller, imposing more stringent demands on the hardware, and the number of shots required to get a reasonable sample size would increase. While the current device hardware is well below the pseudothreshold for the studied circuits, this lack of scalability points to a need to move from error-detecting codes like the $[[4, 2, 2]]$ iceberg code to error-correcting codes like the $[[16, 4, 4]]$ many-hypercube code for applications involving more logical qubits.

B. Many-hypercube code simulation

We also noisily simulate the $[[16, 4, 4]]$ state preparation circuits using Sqalesim with its default parameters (shown in Fig. 14). We observe that our simulations correlate with the measured experimental data (Fig. 8) in that there is a large separation in error rates between the encoded and unencoded. However, the simulation error rates themselves do seem to have slightly less pronounced differences between the unencoded and encoded than in the experiment, suggesting some degree of system drift.

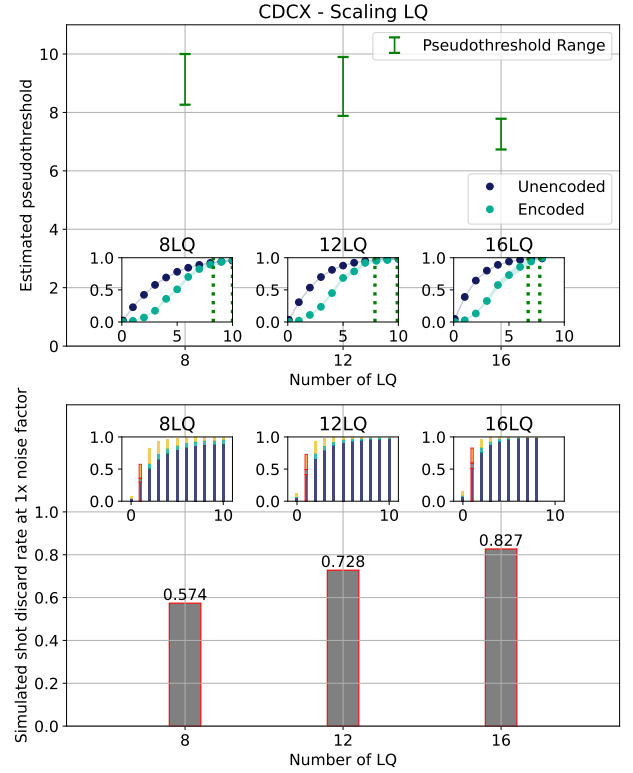


FIG. 13. Scaling of (top) estimated pseudothreshold (error factor at which encoded and unencoded circuit TVDs cross) and (bottom) proportion of shots discarded at $1\times$ noise, as the number of qubits in the CNOT ladder are increased. The insets in the top plot show the TVDs for the encoded and unencoded circuits as all error parameters are scaled, and vertical dotted lines indicating the estimated pseudothreshold range. The insets on the bottom plot show the simulated proportions of shots, color-coded following Fig. 12 discarded as all error parameters are scaled. The bar corresponding to $1\times$ noise is outlined in red.

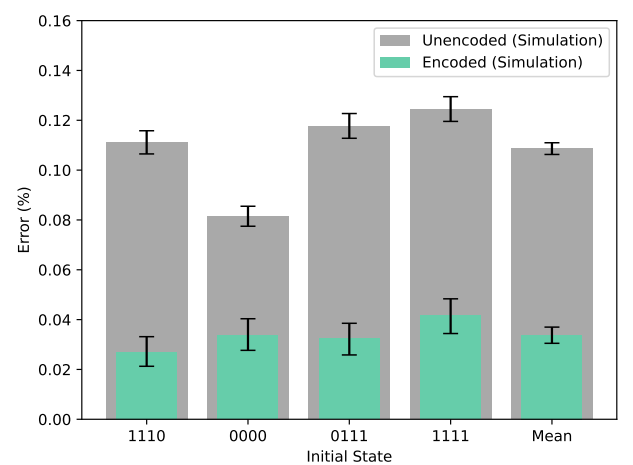


FIG. 14. Noisy error rate simulations of $[[16, 4, 4]]$ state preparation bitstrings executed on hardware.

C. Arbitrary Logical CDCX Circuit

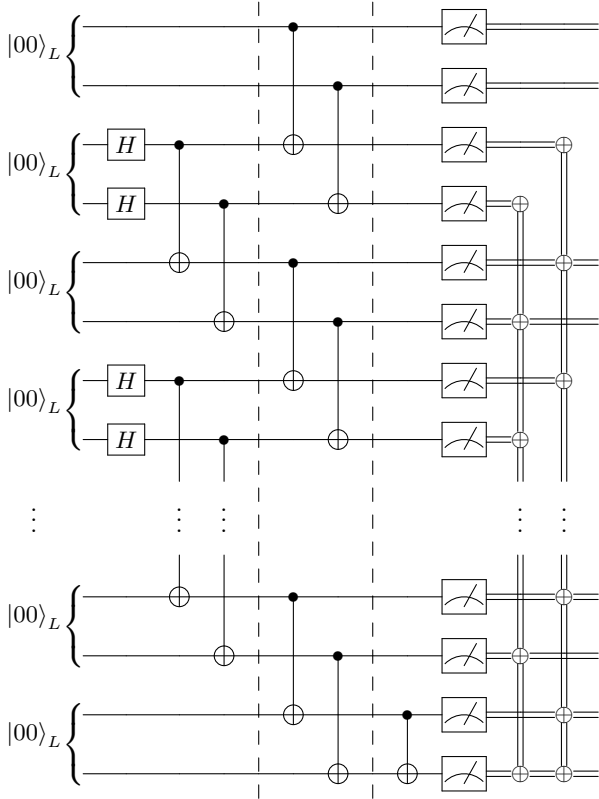


FIG. 15. Arbitrary-length logical constant-depth CNOT ladder. A \oplus on a measured data bit is flipped if the sum (modulo 2) of the measured ancilla bits above it with an \oplus is 1. The qubits with/without a Hadamard applied at the start are ancilla/data qubits, respectively.

D. Shor Loss Correction Results

As discussed in section II C, an additional tool we have in our logical encoding toolkit is that of loss correction. While the circuits executed in section III do not explicitly leverage a dedicated loss-correction gadget at the circuit-level, we can still attempt to infer the loss-corrected outcomes by being aware of the $[[4, 2, 2]]$ codeword structure. Fig. 16 highlights the updated experimental results from section III but with loss correction post-processing enabled (for the logical encodings only, as there is not necessarily a straightforward scheme to exploit for the unencoded circuit outside of guessing). Most notably, and as expected, Fig. 16 shows that loss-correction increases the post-selection yield appreciably, as we discard less of the shots before the logical decoding. However, we also observe that there is a price to pay for this as well. The observed TVDs for the encoded circuits are now higher than before loss correction, albeit still outperforming the unencoded circuit. This is somewhat expected as the inference post-processing is not perfect, accepting, for ex-

ample, shots that may have had multiple logical errors that would have previously been discarded entirely due to any single atom loss. Indeed, it also explains why the performance of the three-row Shor is now more comparable to that of the two-row. There are simply more opportunities to infer a wrong logical codeword with more $[[4, 2, 2]]$ patches, again suggesting that the stronger performance of the three-row Shor is correlated to its additional error detection events. Interestingly, this also has the effect of allowing the two-row Shor LDU circuit to maintain a lower TVD (than its non-LDU variant), as its additional pruning of leakage qubits will allow it to accept less of the potentially faulty loss corrected bitstring outcomes. This highlights a trade-off to consider: is the higher post-selection yield preferable to a minor degradation in TVD (where the criterion for ‘minor’ is maintaining better than unencoded performance)? This trade-off may become more relevant in light of the CZ (or even movement) overhead of an actual loss-correction circuit gadget (similar to the LDU cost observed in the Shor simulations of section IX A 1) or in a shot-constrained scenario where low post-selection yield becomes detrimental – and further preferable if more sophisticated correction post-processing schemes are available to alleviate the apparent TVD (or similar performance metric) degradation.

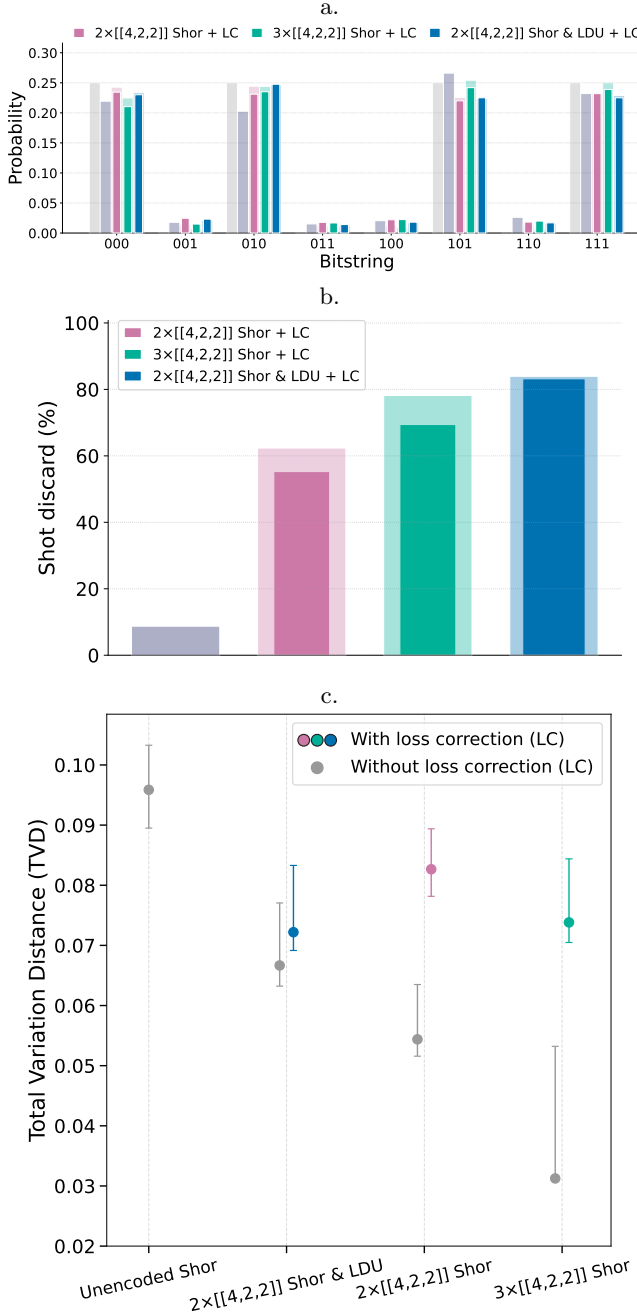


FIG. 16. Updated experimental results for Shor circuits after loss correction (LC) post-processing. The thinner solid bars are loss corrected, while the translucent ones are not (that is, the same data from Fig. 2 for comparison). (a) The updated probability distribution, (b) The updated post-selection discard, and (c) The TVD computed between the experimental and ideal distributions with and without loss correction. Analysis the same as in Fig. 2.

[1] D. Bluvstein, H. Levine, G. Semeghini, T. T. Wang, S. Ebadi, M. Kalinowski, A. Keesling, N. Maskara, H. Pichler, M. Greiner, V. Vuletić, and M. D. Lukin, A quantum processor based on coherent transport of entangled atom arrays, *Nature* **604**, 451–456 (2022).

[2] Suppressing quantum errors by scaling a surface code logical qubit, *Nature* **614**, 676 (2023).

[3] A. Paetznick, M. da Silva, C. Ryan-Anderson, J. Bello-Rivas, J. Campora III, A. Chernoguzov, J. Dreiling, C. Foltz, F. Frachon, J. Gaebler, *et al.*, Demonstration of logical qubits and repeated error correction with better-than-physical error rates, arXiv preprint arXiv:2404.02280 (2024).

[4] M. Bedalov, M. Blakely, P. Buttler, C. Carnahan, F. T. Chong, W. C. Chung, D. C. Cole, P. Goiporia, P. Gokhale, B. Heim, *et al.*, Fault-tolerant operation and materials science with neutral atom logical qubits, arXiv preprint arXiv:2412.07670 (2024).

[5] P. S. Rodriguez, J. M. Robinson, P. N. Jepsen, Z. He, C. Duckering, C. Zhao, K.-H. Wu, J. Campo, K. Baggett, M. Kwon, T. Karolyshyn, P. Weinberg, M. Cain, S. J. Evered, A. A. Geim, M. Kalinowski, S. H. Li, T. Manovitz, J. Amato-Grill, J. I. Basham, L. Bernstein, B. Braverman, A. Bylinskii, A. Choukri, R. DeAngelis, F. Fang, C. Fieweger, P. Frederick, D. Haines, M. Hamdan, J. Hammett, N. Hsu, M.-G. Hu, F. Huber, N. Jia, D. Kedar, M. Kornjača, F. Liu, J. Long, J. Lopatin, P. L. S. Lopes, X.-Z. Luo, T. Macri, O. Marković, L. A. Martínez-Martínez, X. Meng, S. Ostermann, E. Ostroumov, D. Paquette, Z. Qiang, V. Shofman, A. Singh, M. Singh, N. Sinha, H. Thoreen, N. Wan, Y. Wang, D. Waxman-Lenz, T. Wong, J. Wurtz, A. Zhdanov, L. Zheng, M. Greiner, A. Keesling, N. Gemelke, V. Vuletić, T. Kitagawa, S.-T. Wang, D. Bluvstein, M. D. Lukin, A. Lukin, H. Zhou, and S. H. Cantú, Experimental demonstration of logical magic state distillation (2024), arXiv:2412.15165 [quant-ph].

[6] B. W. Reichardt, D. Aasen, R. Chao, A. Chernoguzov, W. van Dam, J. P. Gaebler, D. Gresh, D. Lucchetti, M. Mills, S. A. Moses, *et al.*, Demonstration of quantum computation and error correction with a tesseract code, arXiv preprint arXiv:2409.04628 (2024).

[7] D. Bluvstein, S. J. Evered, A. A. Geim, S. H. Li, H. Zhou, T. Manovitz, S. Ebadi, M. Cain, M. Kalinowski, D. Hangleiter, *et al.*, Architectural mechanisms of a universal fault-tolerant quantum computer, arXiv preprint arXiv:2506.20661 (2025).

[8] D. Bluvstein, S. J. Evered, A. A. Geim, S. H. Li, H. Zhou, T. Manovitz, S. Ebadi, M. Cain, M. Kalinowski, D. Hangleiter, *et al.*, Logical quantum processor based on reconfigurable atom arrays, *Nature* **626**, 58 (2024).

[9] S. Sunami, G. Akihisa, and Y. Hayata, Transversal surface-code game powered by neutral atoms, arXiv preprint arXiv:2506.18979 (2025).

[10] R. Chinnarasu, C. Poole, L. Phuttitarn, A. Noori, T. M. Graham, S. N. Coppersmith, A. B. Balantekin, and M. Saffman, Variational simulation of the Lipkin-Meshkov-Glick model on a neutral atom quantum computer, *PRX Quantum* **6**, 020350 (2025).

[11] J. A. Smolin, G. Smith, and A. Vargo, Oversimplifying quantum factoring, *Nature* **499**, 163 (2013).

[12] H. Goto, High-performance fault-tolerant quantum computing with many-hypercube codes, *Science Advances* **10**, eadp6388 (2024).

[13] E. B. Jones, C. J. Winkleblack, C. Campbell, C. Rotello, E. D. Dahl, M. Reynolds, P. Graf, and W. Jones, Dynamic, symmetry-preserving, and hardware-adaptable circuits for quantum computing many-body states and correlators of the anderson impurity model, arXiv preprint arXiv:2405.15069 (2024).

[14] E. Bäumer and S. Woerner, Measurement-based long-range entangling gates in constant depth, *Phys. Rev. Res.* **7**, 023120 (2025).

[15] D. Litinski, Blocklet concatenation: Low-overhead fault-tolerant protocols for fusion-based quantum computation, arXiv preprint arXiv:2506.13619 (2025).

[16] A. Radnaev, W. Chung, D. Cole, D. Mason, T. Ballance, M. Bedalov, D. Belknap, M. Berman, M. Blakely, I. Bloomfield, P. Buttler, C. Campbell, A. Chopinaud, E. Copenhagen, M. Dawes, S. Eubanks, A. Friss, D. Garcia, J. Gilbert, M. Gillette, P. Goiporia, P. Gokhale, J. Goldwin, D. Goodwin, T. Graham, C. Guttermansson, G. Hickman, L. Hurtley, M. Iliev, E. Jones, R. Jones, K. Kuper, T. Lewis, M. Lichtman, F. Majdeteimouri, J. Mason, J. McMaster, J. Miles, P. Mitchell, J. Murphree, N. Neff-Mallon, T. Oh, V. Omole, C. Parlo Simon, N. Pederson, M. Perlin, A. Reiter, R. Rines, P. Romlow, A. Scott, D. Stiefvater, J. Tanner, A. Tucker, I. Vinogradov, M. Warter, M. Yeo, M. Saffman, and T. Noel, Universal neutral-atom quantum computer with individual optical addressing and nondestructive readout, *PRX Quantum* **6**, 030334 (2025).

[17] C. Campbell, F. T. Chong, D. Dahl, P. Frederick, P. Goiporia, P. Gokhale, B. Hall, S. Issa, E. Jones, S. Lee, *et al.*, Superstaq: Deep optimization of quantum programs, in *2023 IEEE International Conference on Quantum Computing and Engineering (QCE)*, Vol. 1 (IEEE, 2023) pp. 1020–1032.

[18] S. Yoshida, S. Tamiya, and H. Yamasaki, Concatenate codes, save qubits, *npj Quantum Information* **11**, 88 (2025).

[19] R. Stricker, D. Vodola, A. Erhard, L. Postler, M. Meth, M. Ringbauer, P. Schindler, T. Monz, M. Müller, and R. Blatt, Experimental deterministic correction of qubit loss, *Nature* **585**, 207 (2020).

[20] B. W. Reichardt, A. Paetznick, D. Aasen, I. Basov, J. M. Bello-Rivas, P. Bonderson, R. Chao, W. van Dam, M. B. Hastings, R. V. Mishmash, *et al.*, Fault-tolerant quantum computation with a neutral atom processor, arXiv preprint arXiv:2411.11822 (2024).

[21] G. Baranes, M. Cain, J. Ataides, D. Bluvstein, J. Sinclair, V. Vuletic, H. Zhou, and M. D. Lukin, Leveraging atom loss errors in fault tolerant quantum algorithms, arXiv preprint arXiv:2502.20558 (2025).

[22] B. Zhang, G. Liu, G. Bornet, S. P. Horvath, P. Peng, S. Ma, S. Huang, S. Puri, and J. D. Thompson, Leveraging erasure errors in logical qubits with metastable ^{171}yb atoms (2025), arXiv:2506.13724 [quant-ph].

[23] J. Preskill, Reliable quantum computers, *Proc. R. Soc. Lond. A* **454**, 385 (1998).

[24] M. N. H. Chow, V. Buchemavari, S. Omanakuttan, B. J. Little, S. Pandey, I. H. Deutsch, and Y.-Y. Jau,

Circuit-based leakage-to-erasure conversion in a neutral-atom quantum processor, *PRX Quantum* **5**, 040343 (2024).

[25] I. Cong, H. Levine, A. Keesling, D. Bluvstein, S.-T. Wang, and M. D. Lukin, Hardware-efficient, fault-tolerant quantum computation with rydberg atoms, *Physical Review X* **12**, 021049 (2022).

[26] K. Sahay, P.-K. Tsai, K. Chang, Q. Su, T. B. Smith, S. Singh, and S. Puri, Fold-transversal surface code cultivation (2025), arXiv:2509.05212 [quant-ph].

[27] P. W. Shor, Algorithms for quantum computation: discrete logarithms and factoring, in *Proceedings 35th annual symposium on foundations of computer science* (Ieee, 1994) pp. 124–134.

[28] E. Bäumer, V. Tripathi, D. S. Wang, P. Rall, E. H. Chen, S. Majumder, A. Seif, and Z. K. Minev, Efficient long-range entanglement using dynamic circuits, *PRX Quantum* **5**, 030339 (2024).

[29] A. Hashim, M. Yuan, P. Gokhale, L. Chen, C. Juenger, N. Fruitwala, Y. Xu, G. Huang, K. Nowrouz, L. Jiang, *et al.*, Efficient generation of multi-partite entanglement between non-local superconducting qubits using classical feedback, arXiv preprint arXiv:2403.18768 (2024).

[30] K. Temme, S. Bravyi, and J. M. Gambetta, Error mitigation for short-depth quantum circuits, *Physical review letters* **119**, 180509 (2017).

[31] M. Saffman, Quantum computing with neutral atoms, *National Science Review* **6**, 24 (2019).

[32] M. A. Perlin, qLDPC, <https://github.com/qLDPCOrg/qLDPC> (2023).

[33] Y.-C. Zheng, C.-Y. Lai, T. A. Brun, and L.-C. Kwek, Constant depth fault-tolerant clifford circuits for multi-qubit large block codes, *Quantum Science and Technology* **5**, 045007 (2020).

[34] E. Swaroop, T. Jochym-O'Connor, and T. J. Yoder, Universal adapters between quantum ldpc codes, arXiv preprint arXiv:2410.03628 (2024).

[35] L. Z. Cohen, I. H. Kim, S. D. Bartlett, and B. J. Brown, Low-overhead fault-tolerant quantum computing using long-range connectivity, *Science Advances* **8**, eabn1717 (2022).

[36] D. Horsman, A. G. Fowler, S. Devitt, and R. Van Meter, Surface code quantum computing by lattice surgery, *New Journal of Physics* **14**, 123011 (2012).

[37] H. Zhou, C. Zhao, M. Cain, D. Bluvstein, C. Dukering, H.-Y. Hu, S.-T. Wang, A. Kubica, and M. D. Lukin, Algorithmic fault tolerance for fast quantum computing, arXiv:2406.17653 (2024).

[38] M. Serra-Peralta, M. H. Shaw, and B. M. Terhal, Decoding across transversal Clifford gates in the surface code, arXiv preprint arXiv:2505.13599 (2025).

[39] C. Fang, J. Miles, J. Goldwin, M. Lichtman, M. Gillette, M. Bergdolt, S. Deshpande, S. A. Norrell, P. Huft, M. A. Kats, and M. Saffman, Interleaved dual-species arrays of single atoms using a passive optical element and one trapping laser, *Science Advances* **11**, eadw4166 (2025).

[40] M. Saffman, Quantum computing with atomic qubit arrays: confronting the cost of connectivity, arXiv preprint arXiv:2505.11218 (2025).